Reliability Engineering and System Safety 191 (2019) 106571

Contents lists available at ScienceDirect

Reliability Engineering and System Safety

journal homepage: www.elsevier.com/locate/ress

Fragility and risk assessment of aboveground storage tanks subjected to concurrent surge, wave, and wind loads

Carl Bernier, Jamie E. Padgett*

Department of Civil and Environmental Engineering, Rice University, Houston, TX 77005, USA

ARTICLE INFO

Keywords:
Storage tank
Storm surge
Wave
Wind
Fragility model
Risk assessment
Multi-hazard

ABSTRACT

Comprehensive tools to assess the performance of aboveground storage tanks (ASTs) under multi-hazard storm conditions are currently lacking, despite the severe damage suffered by ASTs in past storms resulting in the release of hazardous substances. This paper presents a rigorous yet efficient methodology to develop fragility models and perform risk assessments of ASTs subjected to combined surge, wave, and wind loads. Parametrized fragility models are derived for buckling and dislocation from the ground. The buckling strength of ASTs is assessed using finite element analysis, while the stability against dislocation is evaluated using analytical limit state functions with surrogate modeling-based load models. Scenario and probabilistic risk assessments are then performed for a case study region by convolving the fragility models with hazard models. Results demonstrate that the derived fragility models are efficient tools to evaluate the performance of ASTs in industrial regions. Insights obtained from the fragility and risk assessments reveal that neglecting the multi-hazard nature of storms, as existing studies have done, can lead to a significant underestimation of vulnerability and risks. This paper also highlights how using surrogate model techniques can facilitate and reduce the computational complexity of fragility and risk assessments, particularly in multi-hazard settings.

1. Introduction

Aboveground storage tanks (ASTs) are critical components of oil and gas facilities used to store bulk chemicals. ASTs are typically vertical cylinders constructed from thin steel plates welded together. While this design makes them lightweight and able to resist internal pressure, it also leaves them vulnerable to suffer damage under extreme storm conditions. Damage to ASTs can in turn results in the release of hazardous material; such releases are known as natural hazard-triggered technological (NaTech) events. For example, due to AST failures, more than 26 million liters of oil products were spilled during Hurricanes Katrina and Rita [1], and two million liters of chemicals were released in the Houston region during Hurricane Harvey [2]. Analysis of NaTech events usually identify two main failure modes for ASTs during storms: (i) dislocation from the ground; and (ii) buckling of the tank shell [1,3,4]. Three main hazards can trigger these failure modes. First, high wind velocities can generate severe external loads on ASTs. Storm winds over bodies of water can also generate surge, which then induce hydrostatic and hydrodynamic loads associated with the surge height and current. Lastly, winds can also generate waves atop of the surge, inducing additional hydrodynamic loads depending on the wave heights and periods [4,5].

Given the severe environmental, economic, and social impacts associated with AST damage, the risk assessment of ASTs and NaTech events has become an emerging issue in recent years [4,6–9]. Risk assessments typically requires two main components [7]: (i) a model characterizing the hazard conditions; and (ii) fragility models expressing the likelihood for damage as a function of the AST structural characteristic and hazard conditions. While several studies have developed fragility models for ASTs during earthquake [10–14], lightning [15–17], or even tsunami events [18,19], very few studies have done so for storms. Most of the literature looking at the performance of ASTs during storms have focused on deterministic buckling analysis of ASTs subjected to winds [20], rather than developing fragility models and considering other important loads like storm surge [21]. Landucci et al. [22] presented the first framework to derive fragility models for the buckling of anchored ASTs subjected to flooding or surge. Subsequently, Khakzad and Van Gelder [23,24] proposed a methodology to derive similar models for the buckling and dislocation of unanchored ASTs subjected to flooding or surge and consider the dependencies between failure modes. More recently, Kameshwar and Padgett [21,25] and Zuluaga Mayorga et al. [26] developed fragility models, which are parametrized on the load conditions and AST geometries, for the buckling and dislocation of anchored and unanchored ASTs subjected to

* Corresponding author.
E-mail addresses: carl.bernier@rice.edu (C. Bernier), jamie.padgett@rice.edu (J.E. Padgett).

https://doi.org/10.1016/j.ress.2019.106571
Received 8 February 2019; Received in revised form 21 May 2019; Accepted 7 July 2019
Available online 08 July 2019
0951-8320/

storm surge or wind.

While these studies have provided significant contributions to the safety assessment of ASTs during storms, they developed fragility models for individual loads or hazards (i.e., storm surge or wind), neglecting the multi-hazard nature of storm events and providing an incomplete view of AST vulnerability. An AST exposed to storm surge is expected to be subjected to wind, current and wind-induced waves as well, highlighting the need for more comprehensive models to adequately assess the vulnerability of ASTs during storm events. Beyond fragility assessments, no study has yet proposed a comprehensive framework to perform risk assessments of ASTs located in storm-prone areas, which is further complicated by the need to consider concurrent or multi-hazard loading conditions. Existing risk assessments [7,23,25,27] are limited to individual hazards and primarily rely on deterministic or simplistic storm scenarios, neglecting storm variability. Even for other structures than ASTs and outside the field of NaTech events, the literature is lacking comprehensive fragility and risk assessments for multi-hazard storm conditions. Again, most studies looking at the vulnerability of coastal structures have focused on wind loads alone [28] or surge and wave loads alone [29,30]. Currently, only a few assessments considering multi-hazard storm loads are available for coastal residential structures [5] or wind turbines [31].

This paper aims to: (i) gain a better understanding of the concurrent effects of surge, wave, and wind loads on the vulnerability of ASTs by developing the first fragility models for ASTs subjected to multi-hazard storm conditions; and (ii) illustrate how these fragility models can be coupled with hazard models to perform comprehensive risk assessments. Parametrized fragility models are derived for the two failure modes discussed above, buckling and dislocation. To showcase the application of the derived fragility models in large industrial areas, risk assessments are then performed using a severe storm scenario and, for the first time, a probabilistic storm hazard model capturing concurrent hazard effects on risks to ASTs. The Houston Ship Channel (HSC) in Texas, the largest petrochemical complex in the United States (US), is used as a case study. The tools and methods proposed in this paper will also offer a foundation to perform multi-hazard coastal vulnerability and risk assessments for other structures than ASTs.

The next sections of this paper detail the approach adopted to derive fragility models for ASTs subjected to concurrent storm loads and perform risk assessments. Section 2 defines the load conditions and models employed for the fragility analysis. A model from the literature is adopted for wind, while a surrogate model derived from computational fluid dynamics (CFD) analyses is used for storm surge and waves. Section 3 details the methodology to assess the buckling of ASTs using nonlinear finite element (FE) analysis. Section 4 presents the dislocation analysis of unanchored and anchored ASTs using analytical limit state functions. Section 5 details the methodology to derive the fragility models. Using a statistical sampling method, logistic regression classifiers are trained across ranges of loads and AST modeling parameters. Finally, Section 6 illustrates how scenario-based and probabilistic hazard models can be coupled with the derived fragility models to perform risk assessments.

2. Storm conditions and load models

The development of fragility models first requires an adequate estimation of the load conditions that could occur during storm events. The ranges of load parameters considered in the fragility analysis are detailed in Table 1, while the models employed to estimate surge, wave, and wind loads on ASTs are presented in the next two subsections. Due to a lack of empirical data for oil and gas facilities, numerical simulation of storms around the HSC were performed using *ADCIRC + SWAN* to obtain the parameters in Table 1. *ADCIRC + SWAN* is a computer program that simultaneously solve surge elevations, currents, wave periods, and wave heights to predict the time evolution of surge and wave conditions for a given meteorological forcing [32]. The simulations were executed by the Computational Hydraulics Group at the University of Texas at Austin for Hurricane Ike, which made landfall in the Houston region in 2008, and for two synthetic storms, which correspond to approximately 100- and 500-year storm surge events in the HSC [33]. The synthetic storms are referred to as storm FEMA033 and FEMA036 respectively, and were generated by the Federal Emergency Management Agency (FEMA) as reliable proxies for the hurricane meteorology of the Texas coast given the sparsity of historical records [33]. Surge and wave conditions were then extracted at several industrial sites along the HSC to define the ranges of surge height (S), wave height (H_w), wave period (T_w), and current velocity (U) in Table 1. The range of wind velocity (W) was obtained to be in excess of the design wind speed (76 m/s) for ASTs located along the Texas coast [34].

Table 1
Ranges of load parameters considered for the fragility analysis.

Parameters	Lower bound	Upper bound	Units
Surge height (S)	0.0	7.5	m
Wave height (H_w)	0.2	2.0	m
Wave period (T_w)	3.0	6.0	s
Current velocity (U)	0.0	1.5	m/s
Wind velocity (W)	0.0	100.0	m/s

2.1. Wind load model

Wind pressures (P_w) on ASTs are generally obtained from wind tunnel experiments [20,35] and can be expressed as:

$$P_w(\theta) = p_o C_p(\theta) \tag{1}$$

where p_o is the reference wind pressure, which is equal to $0.5\rho_{air}W^2$ with ρ_{air} being the air density; and C_p is a wind pressure coefficient that vary along the AST circumference (θ; $\theta = 0^\circ$ on the windward side); pressure variations are negligible along the height (z) [35,36]. The pressure coefficient distribution adopted in this study is the one specified by Eurocode EN 1993-4-1 [37] since it has been widely used for wind buckling analysis [25,35]. According to this model, the pressure coefficient is expressed as:

$$\begin{aligned} C_p(\theta) = &-0.54 + 0.16D/H + (0.28 + 0.04D/H)\cos\theta \\ &+ (1.04 - 0.20D/H)\cos 2\theta \\ &+ (0.36 - 0.05D/H)\cos 3\theta - (0.14 - 0.05D/H)\cos 4\theta \end{aligned} \tag{2}$$

where D and H are respectively the AST diameter and height. If $H/D < 0.5$, a value of $H/D = 0.5$ should be used to estimate C_p.

2.2. Storm surge and wave load model

While models are readily available for wind pressures, there is limited information regarding the hydrodynamic pressure (P_d) associated with wave loads and current. Analytical solutions, such as the Morison's equation or diffraction theory [38], are generally not applicable for large-scale cylinders and nonlinear waves, such as ASTs and waves observed during a storm. Instead, numerical methods, such as the finite element (FE) or finite volume method, are usually required for accurate load estimation [39]. However, the use of such numerical methods can be prohibitive for a fragility analysis due to their high computational cost. To overcome this issue, this study relies on a surrogate model of CFD analysis to estimate hydrodynamic pressures on ASTs.

The surrogate model is developed using a set of 240 CFD analyses of ASTs subjected to storm surge and wave loads. The CFD model is detailed in Fig. 1a, adopted from Bernier and Padgett [40], and developed using *LS-Dyna* [41], a commercial FE software. The water and air fluids are governed by the Navier-Stokes equations, while the interface between both fluids is tracked using an Arbitrary Lagrangian-Eulerian

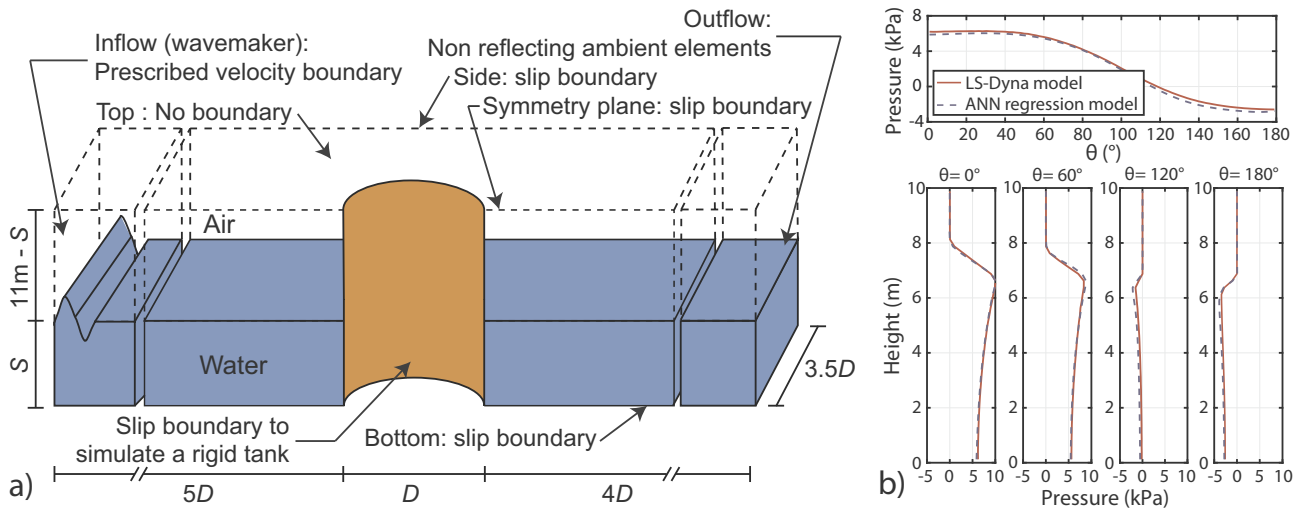

Fig. 1. (a) Overview of the FE model to compute wave loads on ASTs. (b) Pressure distribution and validation of ANN for $D = 15$ m; $H = 10$ m; $S = 6.72$ m; $H_w = 1.35$ m; $T_w = 5.68$ s; $U = 0.15$ m/s.

approach. Waves and current are generated by prescribing the velocity at the inflow boundary. The velocity profiles are obtained from Fenton's wave theory [42] as this theory is appropriate for the conditions listed in Table 1. As detailed in Bernier and Padgett [40], the CFD model was also validated against experimental results. The parameters (i.e., D, S, H_w, T_w, and U) of the 240 CFD analyses are obtained using Latin Hypercube Sampling [43] and the range of load parameters listed in Table 1. For D, a range between 5 and 60 m is assumed based on the AST database presented in [44]. To ensure the generation of realistic waves, a minimum value of 1.0 m is fixed for S and the ratios H_w/S and H_w/λ_w, where λ_w is the wavelength, are limited to 0.65 and 0.14 respectively [42]. For each analysis, the hydrodynamic pressure distribution when the wave force is maximum is extracted around the AST to develop the surrogate model. An example of hydrodynamic pressure distribution is shown in Fig. 1b.

The derived surrogate model consists of an Artificial Neural Network (ANN) as they are powerful regression tools for nonlinear data, such as pressure distributions on structures [45]. An ANN with three layers and 30 log-sigmoid neurons per layer was selected. Out of the 240 CFD analyses, 200 were used to train the ANN, 20 to validate the training and prevent overfitting, and 20 to test its predictive capability. The ANN can estimate the hydrodynamic pressure at any point (θ, z) on the AST as a function of its diameter and the surge and wave conditions (i.e., S, H_w, T_w, and U). On the test data, the ANN predicted the hydrodynamic pressure with a coefficient of determination (R^2) of 0.99 and an average error of 5.4%. Fig. 1b also shows the performance of the ANN for conditions not seen before by the surrogate model. Moreover, less than 0.3 s is required to estimate the hydrodynamic pressure distribution with the ANN, compared to a minimum of 30 CPU hours with the CFD model. These results highlight the adequacy of the surrogate model to efficiently estimate surge and wave loads, and facilitate the fragility analysis presented in the next sections. Additional details on the ANN can be found in Bernier and Padgett [46].

3. Buckling analysis

Buckling is one of the main failure modes for ASTs during storm events and occurs when excessive water or wind pressures act on an AST [1,3], leading to severe deformations of the tank shell, and ultimately to the rupture of the AST. Buckling is of concern for ASTs anchored to the ground; unanchored ASTs generally dislocate before buckling can occur [21,47]. Even though ASTs are not commonly anchored in coastal regions, like the Gulf Coast [44], buckling is still relevant to evaluate the vulnerability of regions where ASTs could actually be anchored and to evaluate the effects of anchoring as part of mitigation plans [25]. The buckling strength of ASTs is assessed here by using FE analysis. First, for a given AST, the structural characteristics (i.e., shell courses, stiffening rings, and roof properties) are determined in accordance with the American Petroleum Institute (API) Standard 650 [48]. Only ASTs with a conical roof are considered in this study. Next, a FE model of the AST is developed in *LS-Dyna* as illustrated in Fig. 2a. The courses and roof are modeled with shell elements, while the roof rafters and stiffening rings with beam elements. The tank shell is fixed to the ground to simulate anchored ASTs and the potential for uplift of the baseplate is neglected. It is acknowledged that this assumption might affect the buckling strength of ASTs [49]. The modeling of the flexibility between the baseplate and the tank shell is outside the scope of this study, but offers interesting future research possibilities.

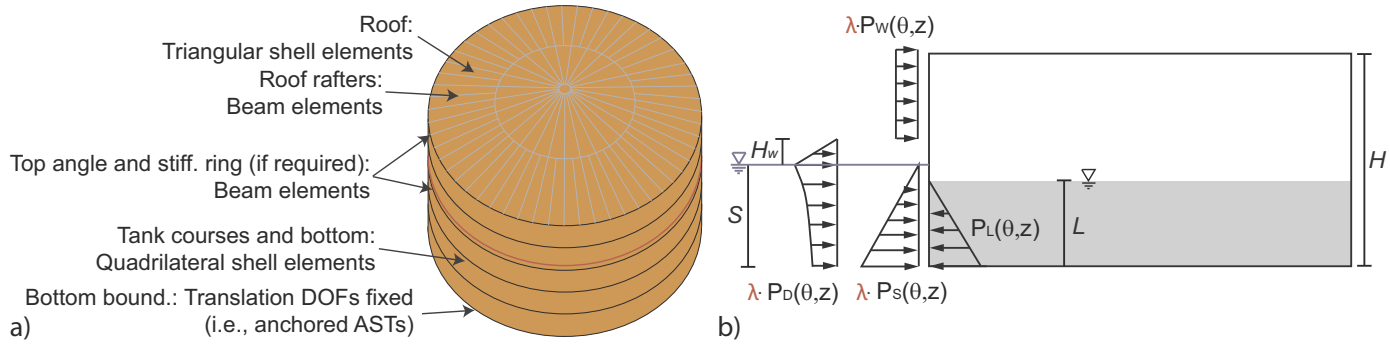

Fig. 2. (a) FE representation of an AST for buckling analysis; (b) Schema of loads acting on an AST for buckling analysis.

An elastoplastic material model with the properties of steel is assigned to all elements. The FE model considers both material and geometric nonlinearities, as well as the global geometric imperfections of the tank shell. The global geometric imperfections are defined using the model proposed by Kameshwar and Padgett [50].

The loads considered for the buckling analysis are summarized in Fig. 2b. The hydrostatic pressure of the surge (P_s), characterized by S and the water density (ρ_w), and the internal liquid pressure (P_L), characterized by the internal liquid height (L) and the internal liquid density (ρ_L), are modeled using triangular distributions. The hydrodynamic pressure is obtained from the ANN model presented in Section 2.2, while the wind pressure acting on the dry section of the AST is obtained from Eqs. (1) and (2). Despite their transient nature, wind and wave loads are applied statically. Previous studies have shown that the buckling strength of ASTs is not significantly affected by wave and wind dynamic effects [40,51]; differences less than 5% are observed between static and dynamic estimates. Also, this modeling error can be easily propagated as detailed below.

For a given combination of load parameters (i.e., S, H_w, T_w, U, W, L, and ρ_L), the external pressures applied on the AST are scaled by a load factor (λ). Nonlinear static analyses are then performed for increasing values of λ until loss of stability occurs. Loss of stability is characterized by a jump in the AST response for a small increase of λ [51]; the value of λ at that point is the critical load factor (λ_{cr}). The condition of AST buckling can then be assessed using the limit state function in Eq. (3); the AST buckles if the external loads are not fully developed when loss of stability occurs.

$$g_{buckling} = (\lambda_{cr} + \varepsilon_{\lambda-\text{stat}} + \varepsilon_{\lambda-\text{ANN}}) - 1 < 0 \tag{3}$$

In this equation, $\varepsilon_{\lambda\text{-stat}}$ is an error term related to the use of a static analysis for dynamic loads, whereas $\varepsilon_{\lambda\text{-ANN}}$ represents the error associated with the ANN to estimate the hydrodynamic pressure for the buckling analysis. The error terms are modeled with the probability distributions presented in Table 2 and the derivation can be found in [40] for $\varepsilon_{\lambda\text{-stat}}$ and [46] for $\varepsilon_{\lambda\text{-ANN}}$.

4. Dislocation analysis

Another failure mode is the dislocation of ASTs from the ground. Storm surge effects are generally responsible for the dislocation of ASTs, but wind loads could also facilitate this failure mode [1]. Dislocation can result in the release of the AST's internal content due to the rupture of connected pipes or impacts with obstacles. Dislocation of unanchored or anchored ASTs can occur under three different mechanisms: uplift, sliding, or overturning. As shown in Eqs. (4) to (6) and schematized in Fig. 3, the limit state functions for the three mechanisms can be expressed as sums of forces and moments and evaluated analytically. Assuming a series system, dislocation occurs if any of Eqs. (4) to (6) is below 0.

$$g_{uplift} = W_t + W_L - F_b - F_u + \sum_{i=1}^{N_a} T^*_{a,i}\cdot \text{I}[\text{Anchor}_i | T_{a,i}, V_{a,i}] < 0 \tag{4}$$

Table 2
Error or bias removal terms considered in the fragility analysis.

Source of uncertainty	Distribution
Error of static analysis on λ_{cr} ($\varepsilon_{\lambda\text{-stat}}$)	Normal(−0.03, 0.03)
Error of ANN on λ_{cr} ($\varepsilon_{\lambda\text{-ANN}}$)	Normal(−0.01, 0.03)
Error of ANN on F_{hd} (ε_{Fd})	Normal(1.00,0.04)
Error of ANN on M_{hd} (ε_{Md})	Normal(1.00, 0.06)
Anchor bias removal T_{c1} (ε_1)	Normal(0.99, 0.18)
Anchor bias removal T_{c2} (ε_2)	Normal(1.04, 0.26)
Anchor bias removal T_{cb} (ε_3)	Normal(0.96, 0.19)
Anchor bias removal V_c (ε_4)	Normal(0.96, 0.16)

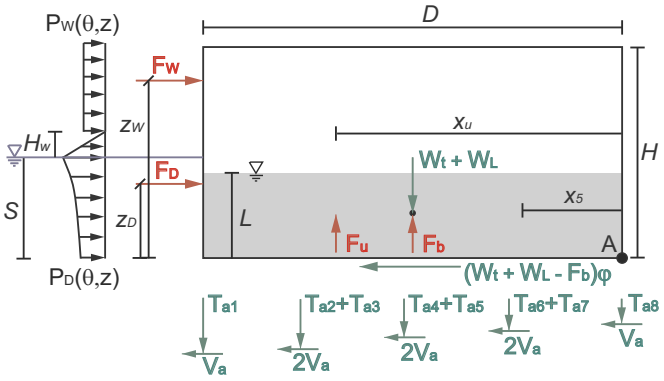

Fig. 3. Schema of loads and forces acting on ASTs for the dislocation analysis.

$$g_{sliding} = (W_t + W_L - F_b - F_u)\cdot\varphi - \varepsilon_{Fd}F_d - F_W + \sum_{i=1}^{N_a} V^*_{a,i}\cdot \text{I}[\text{Anchor}_i | T_{a,i}, V_{a,i}] < 0 \tag{5}$$

$$g_{overturning} = (W_t + W_L - F_b)\cdot D/2 - \varepsilon_{Md}M_d - M_W - M_u + \sum_{i=1}^{N_a} T^*_{a,i}\cdot x_i \cdot \text{I}[\text{Anchor}_i | T_{a,i}, V_{a,i}] < 0 \tag{6}$$

In Eqs. (4) to (6), W_t is the tank weight computed by estimating the tank thickness per the API 650 standard; $W_L = \pi g \rho_L L D^2/4$ is the internal liquid weight; $F_b = \pi g \rho_w S D^2/4$ is the buoyant force from the surge; φ is the friction coefficient at the AST foundation; F_d and M_d are the horizontal force and moment obtained by integrating the hydrodynamic pressure distribution from the ANN model in Section 2.2; F_W and M_W are the horizontal force and moment obtained by integrating the wind pressure distribution from Eqs. (1) and (2) on the dry surface of the AST; F_u and M_u are the vertical force and moment from the uplift generated by the waves and obtained by integrating the hydrodynamic pressure at the base of the AST; ε_{Fd} and ε_{Md} are error terms detailed in Table 2 that propagate the error associated with the ANN when estimating F_d and M_d [46]; N_a is the number of anchors, if any; x_i is the lever arm of anchor i as shown in Fig. 3; $T^*_{a,i}$ and $V^*_{a,i}$ are the maximum allowable tensile and shear forces in anchor i; and $\text{I}[\text{Anchor}_i | T_{a,i}, V_{a,i}]$ is an indicator function equal to 0 if anchor i fails under tensile force $T_{a,i}$ and shear force $V_{a,i}$.

According to Eligehausen et al. [52], the failure of an anchor subjected to combined tensile and shear forces (T_a and V_a) can be determined from the following inequality:

$$(T_a/T_r)^{1.5} + (V_a/V_r)^{1.5} > 1.0 \tag{7}$$

where T_r and V_r are the tensile and shear strength of the anchor. The maximum allowable tensile force (T^*_a) is the value of T_a such that Eq. (7) is equal to 1.0 knowing T_r, V_a, and V_r; V^*_a is obtained similarly. The tensile strength of an anchor is the minimum value of the steel tensile strength (T_s), concrete cone strength with sufficient (T_{c1}) and insufficient (T_{c2}) edge distance, and side face blowout strength (T_{cb}) as shown in Eq. (8), whereas the shear strength is the minimum of the steel shear strength (V_s), concrete edge strength (V_c), and pryout strength (V_{cp}) as shown in Eq. (9).

$$\begin{aligned} T_r &= \min(T_s, T_{c1}, T_{c2}, T_{cb}) \\ T_s &= 1.9 A_s f_y \\ T_{c1} &= \varepsilon_1 16.8 h_{ef}^{1.5} f_c^{0.5} \\ T_{c2} &= \varepsilon_2 (A_{C,N}/A^0_{C,N}) \Psi_{S,N} T_{c1} \\ T_{cb} &= \varepsilon_3 20.9 c^{0.75} A_h^{0.5} f_c^{0.75} \end{aligned} \tag{8}$$

$$\begin{aligned} V_r &= \min(V_s, V_c, V_{cp}) \\ V_s &= 1.14 A_s f_y \\ V_c &= \varepsilon_4 3.25 d^{\alpha} h_{ef}^{\beta} f_c^{0.5} c^{1.5} \\ V_{cp} &= 2.0 \min(T_{c1}, T_{c2}) \end{aligned} \quad (9)$$

In the above equations, d is the anchor diameter; A_s is the anchor bolt area; A_h is the anchor head area; f_y is the steel yield strength; f'_c is the concrete strength; h_{ef} is the embedment depth; c is the edge distance; α, β, $\Psi_{S,N}$, and $A_{C,N}/A^0_{C,N}$ are coefficients found in [52]; and ε_1, ε_2, ε_3, and ε_4 are bias modification factors to consider that the relations in Eqs. (8) and (9) do not perfectly fit the experimental data used to derive them [52].

For unanchored ASTs, Eqs. (4) to (6) are readily evaluated by neglecting the anchors term to determine if dislocation occurs for a given combination of load parameters. For anchored ASTs, Eqs. (4) to (6) are first evaluated by assuming that all anchors are present. The loads in each anchor are then computed and Eq. (7) is verified for each anchor. The shear load is equally divided among all anchors, while the tensile loads in each anchor is evaluated through a sum of forces and moments with respect to point A in Fig. 3. To determine the tensile loads, the AST is assumed to behave rigidly (i.e., loads proportional to the lever arm), the anchors are symmetrically distributed with respect to the wave and wind direction, and anchors with the same lever arm have the same tensile and shear strength. These assumptions were validated in Bernier [47]. If a row of anchors fails, the tensile and shear load is redistributed in the remaining anchors and Eq. (7) is verified again. This process is repeated until all anchors fail or no additional anchor fails.

5. Fragility assessment

With the above methods to assess buckling and dislocation, parametrized fragility models can be developed. Parametrized fragility models provide the probability of failure as a function of a set of load parameters (***IM***) and a set of AST parameters (***X***), and can be readily applied for any geometry, internal liquid properties, or surge, wave, and wind conditions. The methodology to derive the buckling and dislocation fragility models is summarized in Fig. 4; each model is developed separately.

First, LHS is employed to generate training and test samples that span the space of load and AST parameters. The load parameters are the ones in Table 1, while the AST parameters are presented in Table 3. Not all AST parameters are required to develop a given fragility model. For instance, the buckling fragility model only requires the five first AST parameters, while the dislocation fragility model for anchored ASTs requires all of them. The ranges of geometry and internal liquid properties were obtained from [44]; the design stress (S_d), which defines the yield strength and is one of the parameters determining the tank thickness, from [48]; the coefficient of friction from [53,54]; and the anchor parameters from [48,52]. For each sample, the structural characteristics required to assess buckling and dislocation are obtained by assuming that the AST conforms to the API 650 Standard. Then, the surge, wave, and wind loads are estimated according to Section 2, and the limit state functions are evaluated to determine if the sample survived or failed. For dislocation, Eqs. (4) to (6) are evaluated directly. For buckling, λ_{cr} is obtained through a FE analysis before evaluating Eq. (3). Using the binary output of the training samples, the fragility model is derived using logistic regression as shown in Eq. (10).

$$P(\text{Failure}|\mathbf{IM}, \mathbf{X}) = \frac{1}{1 + \exp(-l(\mathbf{IM}, \mathbf{X}))} \quad (10)$$

In the above equation, ***l(IM,X)*** is a logit function that expresses the log-odds of failure and is obtained through stepwise regression. The logit functions for the different fragility models derived here can be found in the Supplementary Material. Finally, the accuracy of the classifier is assessed using the test samples; the number of test samples is 10% of the number of training samples. If the accuracy is inadequate, the number of training samples can be increased or a different classification algorithm can be used.

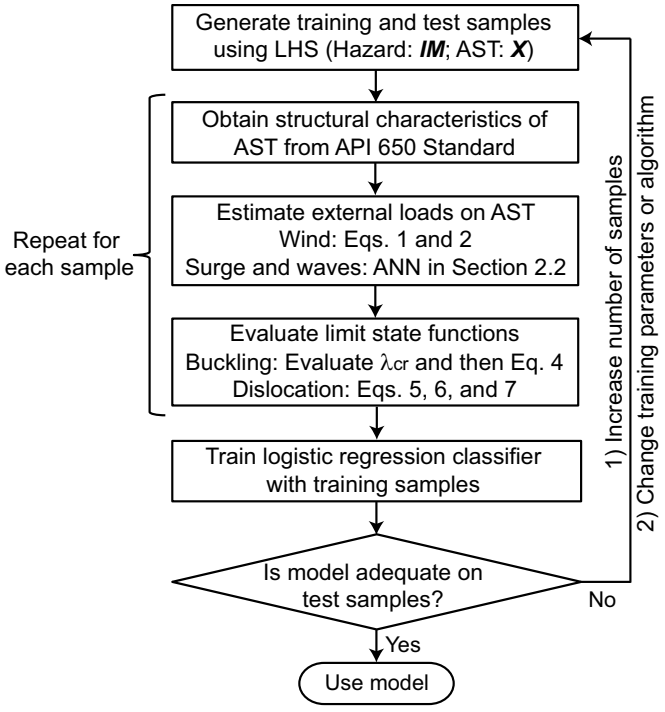

Fig. 4. Overview of methodology to derive buckling and dislocation fragility models.

Table 3
Ranges of modeling parameters considered to develop the fragility models.

Parameters	Lower bound	Upper bound	Units
Diameter (D)	5	60	m
Relative height (H/D)	$\exp((1-2\ln D)/4)$	$\exp(3-0.95\ln D)$	–
Relative internal liquid height (L/H)	0.0	0.9	–
Internal liquid specific gravity (ρ_L)	0.5	1.0	–
Design stress (S_d)	137	196	MPa
Coefficient of friction (φ)	0.3	0.7	–
Anchor steel strength (f_y)	250	550	MPa
Foundation steel strength (f'_c)	20	40	MPa
Anchor edge distance (c)	0.05	0.3	m
Anchor embedment depth (h_{ef})	0.15	0.9	m
Anchor diameter (d)	12.5	50	mm
Anchor spacing (s)	0.3	3.0	m

Using the above methodology, the fragility models are derived by assuming that all loads acting on ASTs are uncorrelated. While surge, wave, and wind loads are expected to be correlated, this correlation is typically site- and storm-dependent. The approach used here generates more general models that efficiently cover all the combinations of load conditions that reasonably could be encountered. Nonetheless, hazard correlations should be considered when integrating the fragility models with hazard models in a risk assessment.

5.1. Buckling fragility model

The first fragility model developed here is for the buckling of anchored ASTs subjected to concurrent surge, wave, and wind loads. A total of 6000 samples were generated to derive the fragility model; 5400 for training and 600 for testing. The logit function is presented in Table S2 in the Supplementary Material. On the test samples, the

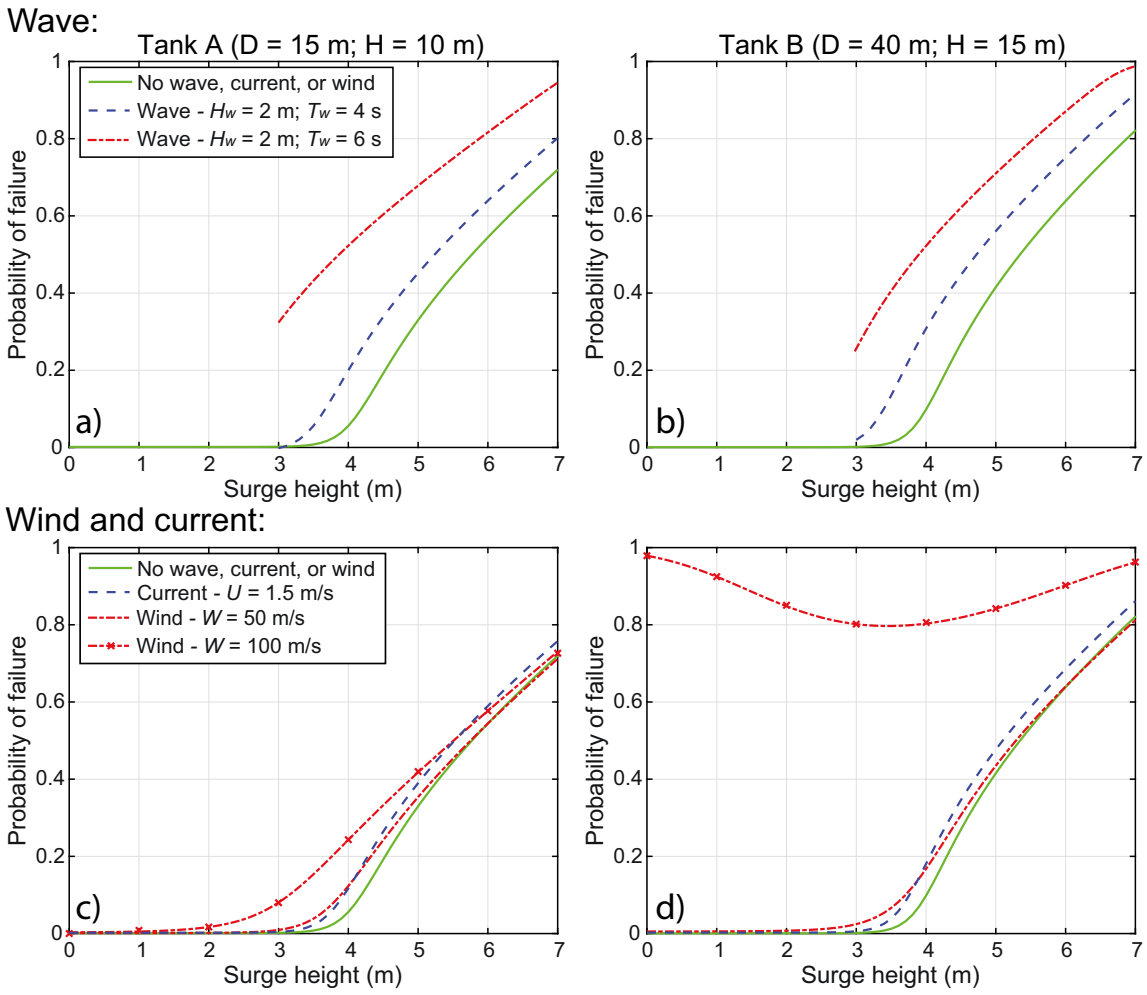

Fig. 5. Effects of load parameters on the buckling fragility of two case study anchored ASTs. Wave height and period: (a) Tank A; (b) Tank B. Wind and current velocity: (c) Tank A; (d) Tank B.

accuracy of the buckling fragility model is of 94.3%. The effects of varying the load parameters on the probability of buckling are presented in Fig. 5 for a slender AST, Tank A (D = 15 m and H = 10 m), and a broad AST, Tank B (D = 40 m and H = 15 m). Based on analyses across range of geometries, the overall results obtained for Tank A are representative of ASTs with diameter between 5 and 25 m and aspect ratio (H/D) between 0.6 and 1.5, while they are representative of diameter between 30 and 60 m and aspect ratio between 0.25 and 0.5 for Tank B. Using the buckling fragility model requires knowledge of the all conditioning parameters. However, if some parameters are uncertain, it is possible to condition the fragility model on a subset of parameters by convolving Eq. (10) over the probability density functions of the uncertain parameters as detailed in Section 6.1. This approach was employed to obtain Fig. 5, where the fragility model is only conditioned on S; D, H, H_w, T_w, U, and W are fixed to the values shown in Fig. 5; ρ_L and S_d are fixed at 0.75 and 160 MPa respectively; and L is uniformly distributed with the bounds shown in Table 3.

Fig. 5 provides key insights to better understand the vulnerability of ASTs to buckling during storm events. Fig. 5a and b show the effects of wave loads for Tanks A and B respectively. As observed, the two ASTs become vulnerable to buckling for surge heights above 3 m, and considering wave loads can increase the probability of failure by up to 40%, highlighting the significant effects of waves on the buckling performance of ASTs. Also, Tank B is slightly more vulnerable to buckling than Tank A, especially for high surge height. Generally, as the AST diameter increases and the aspect ratio decreases, compressive stresses induced by surge and wave loads become significantly higher in the lower-half of the AST, facilitating buckling. Fig. 5c and d show the effects of current and wind velocity for Tanks A and B respectively. Considering current or a wind velocity of 50 m/s affects the probability of buckling by less than 5%. However, a wind velocity of 100 m/s can increase the probability of failure by 10 to 20% for Tank A, while it can cause the buckling of Tank B even when no surge acts on it. Additional analysis indicates that no significant interactions between waves, current, or wind exists, except if high wind velocities are expected. The limited effect of current is due to the relatively small pressures associated with the range of velocity in Table 1. For wind, the limited effect is due to the fact that ASTs conforming to the API 650 Standard are designed for wind loads, but are not designed for storm surge and waves [48]. However, for velocities above the design value, buckling is possible and wind loads become critical.

5.2. Dislocation fragility models

For the dislocation of ASTs due to surge, wave, and wind loads, two fragility models are derived: one for unanchored ASTs and one for anchored ASTs. A total of 10,000 samples were used for unanchored ASTs, while 20,000 samples were used for anchored ASTs; for both models, 10% of the samples are reserved for testing. The logit functions are presented in Tables S3 and S4 in the Supplementary Material for unanchored and anchored ASTs respectively. The accuracy of the models on the test samples is 98.8% and 97.6% for the unanchored and

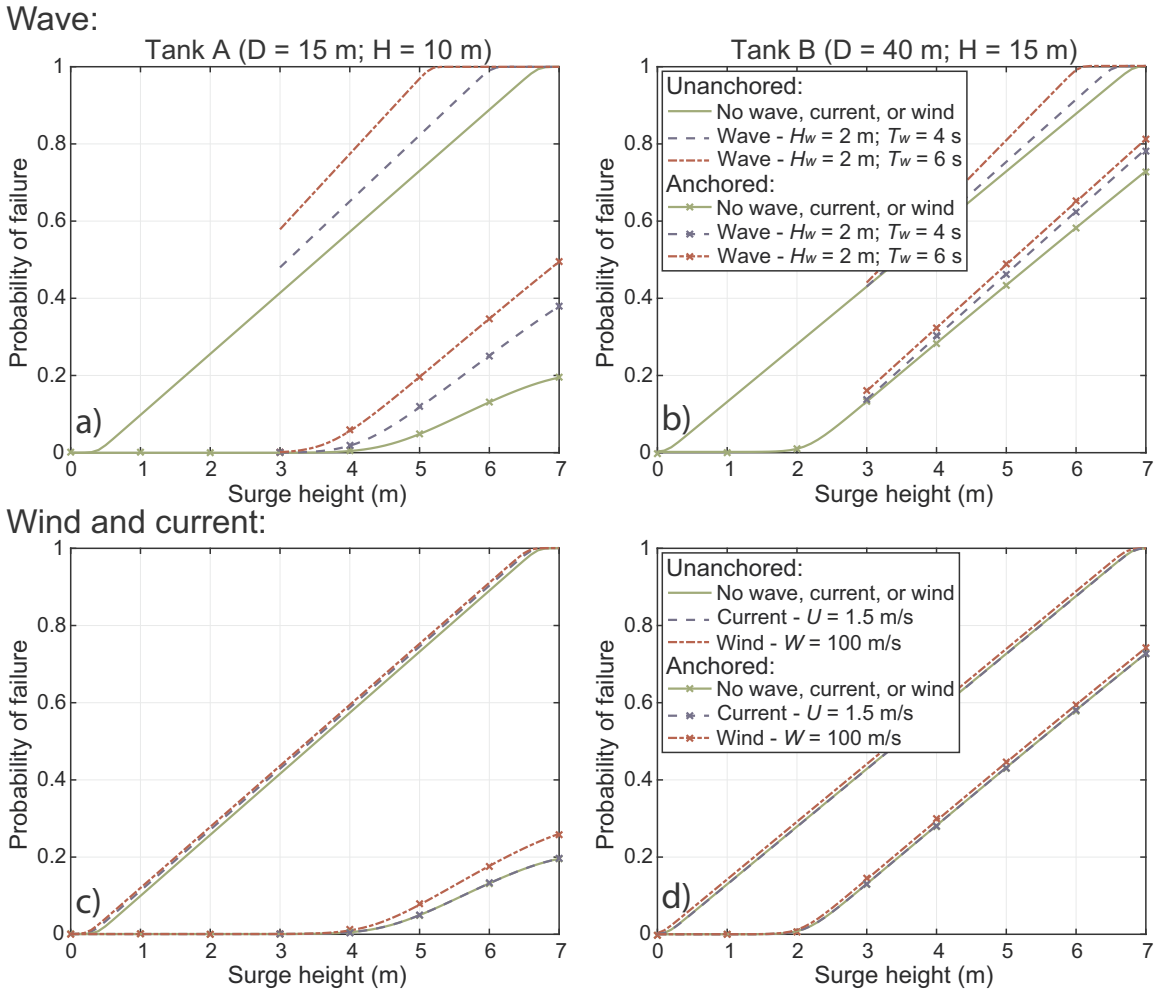

Fig. 6. Effects of load parameters on the dislocation fragility of two case study ASTs. Wave height and period: (a) Tank A; (b) Tank B. Wind and current velocity: (c) Tank A; (d) Tank B.

anchored models respectively.

Fig. 6 illustrates the effects of the different load parameters on the probability of dislocation of Tanks A and B. This figure was generated using the same methodology as Fig. 5; the curves for anchored ASTs assume $f_y = 400\,\text{MPa}$, $f'_c = 30\,\text{MPa}$, $c = 0.1\,\text{m}$, $h_{ef} = 0.3\,\text{m}$, $d = 25.4\,\text{mm}$, and $s = 1.0\,\text{m}$. Fig. 6 first presents useful insights, especially for risk mitigation, regarding the effects of anchors. As observed, anchors significantly reduce the likelihood of dislocation for slender ASTs like Tank A, while the effect is more limited for broad ASTs like Tank B given the larger uplift and lateral forces acting on them; anchorage might not be an optimal measure to prevent the dislocation of broad tanks. For similar reasons, in practice, slender ASTs are the ones typically anchored to the ground, while broad ASTs are generally not. With respect to the effects of concurrent loads, Fig. 6a and b indicates that waves are more critical for slender ASTs than for broad ones. The larger self-weight and diameter of broad ASTs prevents sliding and overturning, leaving them primarily vulnerable to uplift. For Tank A, considering wave loads can increase the probability of dislocation by up to 25% if the tank is unanchored or 30% if the tank is anchored to the ground. Wave loads typically have a larger effect on anchored ASTs than unanchored ASTs. For small anchored ASTs, overturning can become more likely since anchors partially prevent uplift, increasing the relative effects of lateral loads to induce failure. Fig. 6c and d indicate that current and wind loads have a very limited effect on the likelihood of dislocation for both case study ASTs. Similar to buckling, current and wind forces are significantly smaller than wave and uplift forces, and ASTs are designed to resist wind loads. Overall, the results presented in Figs. 5 and 6 highlight the potential importance of considering the concurrent effects of storm loads to adequately assess the structural vulnerability of ASTs during storm events.

6. Application of fragility models for the risk assessment of industrial regions

One of the main applications of fragility models is to perform risk assessments of industrial areas prone to storm events. The Houston Ship Channel is employed here to illustrate how the derived fragility models can be coupled with storm hazard models to perform such risk assessments. Located in the hurricane-prone Gulf Coast area, the HSC is the largest petrochemical complex in the US, with more than 4600 ASTs. Two risk assessments are performed, one using a deterministic scenario and one using a probabilistic hazard model. The locations, ground elevations, containment berm heights, dimensions (D and H), and ranges of internal liquid density for all ASTs located in the HSC are obtained from Bernier and Padgett [44]. For illustration purposes, only the unanchored dislocation fragility model is employed. Nonetheless, the frameworks presented below could also use the buckling and anchored dislocation models to assess risk in regions where ASTs are anchored or to assess the potential effects of mitigation strategies on risk.

6.1. Scenario-based risk assessment

The scenario-based risk assessment is performed for the synthetic storm presented in Section 2 that approximately corresponds to 500-year surge elevations in the HSC (i.e., Storm FEMA036). From the *ADCIRC + SWAN* simulation, the surge height, significant wave height (H_s), peak wave period (T_p), current velocity, and 10-min averaged wind velocity time histories were extracted at each AST location. To use the fragility model, H_s and T_p are converted to maximum wave height and corresponding wave period using the statistical relations presented in Elfrink et al. [55], while the wind velocities are converted to 3-s gust winds using the gust factors found in [56]. When evaluating the loads for an AST, the presence of a containment berm is also considered. If the surge height is less than the berm height, no surge, current, or wave loads act on the ASTs.

The conditional probability of failure at a given timestep t during a storm is evaluated as:

$$P(\text{Failure}|\mathbf{IM},\mathbf{X}_1) = \int_{\mathbf{X}_2} P(\text{Failure}|\mathbf{IM},\mathbf{X}_1, \mathbf{x}_2) f_{\mathbf{X}_2}(\mathbf{x}_2) d\mathbf{x}_2 \quad (11)$$

In this equation, $\boldsymbol{IM}$ is the set of load parameters extracted at the AST location at time t; $\boldsymbol{X_1}$ is the set of known AST parameters; $\boldsymbol{X_2}$ is the set of uncertain AST parameters; $f_{\boldsymbol{X2}}(\boldsymbol{x_2})$ is the joint probability distribution (JPD) of the uncertain parameters; and $P(\text{Failure}|\boldsymbol{IM, X_1, X_2})$ is the unanchored dislocation fragility model. While the geometry and design of ASTs are known prior to a storm (i.e., $\boldsymbol{X_1} = \{D, H, S_d\}$), the contents and internal liquid levels are usually uncertain before a storm. Also, the coefficient of friction is unknown due to a lack of information, leading to $\boldsymbol{X_2} = \{L, \rho_L, \varphi\}$. The three uncertain parameters are modeled as independent uniform random variables. The lower and upper bounds for L and φ are the one in Table 3, while the bounds for ρ_L are obtained from [44] for each AST. Eq. (11) is evaluated here using Monte Carlo simulations (MCS) with 10,000 samples. In the case of anchored ASTs, Eq. (11) should be evaluated using a series system assumption with the buckling and anchored dislocation fragility models [25].

Since storms are long duration events, Eq. (11) is evaluated at each 1-hour timestep of Storm FEMA036; the duration of the storm is of approximately 24 h. The probabilities obtained from Eq. (11) correspond to the probability of failure at time j given that the AST survived before time j. To capture the fact that failure could occur at any timestep during a storm, time-dependent reliability, as detailed in Masoomi et al. [5], is employed to compute the probability that the AST is in a failed state at the end of the storm. This methodology was repeated for all ASTs located in the HSC to obtain the map presented in Fig. 7a.

While the map shown in Fig. 7a indicates the locations of vulnerable ASTs, it does not provide any information on the potential consequences of AST failures. To better evaluate risks, the expected spill volumes for each AST are computed by introducing the internal liquid volume (i.e., $\pi LD^2/4$) in the integral of Eq. (11) and assuming that ASTs will spill their entire contents if failure occurs. Since this assumption is conservative, the spill volumes obtained in this study may not represent accurate estimates of spills that could occur during an event [44]. However, the expected spill volume represents a more reliable proxy for risks than the probability of failure alone. The expected spill volume can distinguish the fact that, depending on their geometries, ASTs with the same probability of failure might not lead to the same consequences. The expected spill volumes are computed at each timestep, and again time-dependent reliability is used to obtain values over the timeframe of the storm.

Table 4 presents the expected spill volume of all ASTs in the HSC as well as the number of ASTs with a high probability of being in a failed state ($P_f > 0.75$) at the end of the storm for different load combinations. Results indicate that the hydrostatic effects of the surge account for approximately 90% of the spill volume when all loads are considered since ASTs are assumed unanchored and uplift is the main failure mechanism. Considering wave loads can increase the spill volume by 10% and the number of highly vulnerable ASTs by 20%. The effects of wind and current are minimal ($\approx 1\%$) on the spill volume and number of highly vulnerable ASTs as wind velocities are below the design value and current velocities below 0.5 m/s during this storm. As observed in the second part of Table 4, large ASTs ($D > 25$ m) account for less than 10% of the highly vulnerable ASTs. However, they account for 70% of the spill volume even though they represent only 30% of the total number of ASTs, highlighting the larger consequences associated with such ASTs. Most of the highly vulnerable ASTs are small ASTs given their limited ability to resist dislocation. The large jump in the number of highly vulnerable ASTs when considering wave and wind loads is also primarily attributed to small size ASTs given their limited ability to resist sliding and overturning. Overall, the results presented in Table 4 generalize the findings obtained in Fig. 6 to a large-scale portfolio of ASTs. Considering concurrent storm loads, especially wave loads, is essential to adequately assess risks during a severe event.

6.2. Probabilistic risk assessment

While scenario-based risk assessments can provide useful information, they do not propagate the uncertainties associated with the hazards and their results are limited to a single deterministic event. In order to consider the ranges of storm conditions that could be expected at a given location and obtain more holistic measures of risks, probabilistic risk assessments are necessary. Performing a probabilistic risk assessment requires evaluation of the probability of failure for a large number of storm scenarios. As detailed in Sections 2 and 6.1, storm conditions for a given scenario are usually determined using computationally expensive numerical models, such as *ADCIRC + SWAN*, creating a constraint for probabilistic assessment. To alleviate this computational constraint, this study relies on surrogate models to approximate storm conditions at AST locations. The surrogate models are derived using a set of 223 synthetic storms developed by FEMA for the Upper Texas Coast and modeled by the US Army Corps of Engineers (USACE) [57]; Storm FEMA036 is part of this set. The storms are characterized by a set of five parameters ($\boldsymbol{\omega}$): (i) the landfall location (x_o); (ii) the angle of approach at landfall (ϕ); (iii) the pressure deficit (Δ_p), which defines the storm intensity; (iv) the radius of maximum wind (R_m), which defines the storm size; and (v) the storm's forward speed (V_f).

At each AST location in the HSC, the surge and wave conditions are extracted for the 223 storms; the surge and wave conditions fall within the ranges listed in Table 1 and used to derive the fragility models. The surrogate models are then derived using Kriging regression and the methodology proposed by Jia and Taflanidis [58]. The Kriging models are trained using *UQLab* [59] and leave-one-out (LOO) cross-validation. Three separate surrogate models are developed to predict at each AST location: (i) the maximum surge height as a function of the storm parameters (i.e., $S(\boldsymbol{\omega})$); (ii) the corresponding significant wave height ($H_s(\boldsymbol{\omega})$); and (iii) the corresponding peak period ($T_p(\boldsymbol{\omega})$). As the wind and current outputs cannot be obtained for the suite of storms as provided [57], no surrogate models were derived for W and U. Based on the findings in Section 6.1, neglecting wind and current should not significantly affect the results of the risk assessment. The performance of the three surrogate models in term of averaged R^2 and mean LOO errors is presented in Table 5 [58], highlighting the adequacy of the Kriging models to efficiently approximate surge and wave conditions at AST locations.

With the above surge and wave hazard surrogate models as well as with knowledge of the annual rate of occurrence of storms (μ) and the JPD of storm parameters ($f_\Omega(\boldsymbol{\omega})$), the annual probability of failure of an AST can be estimated using Eq. (12). This equation is inspired by the approach used by the USACE for their coastal hazard assessments [57].

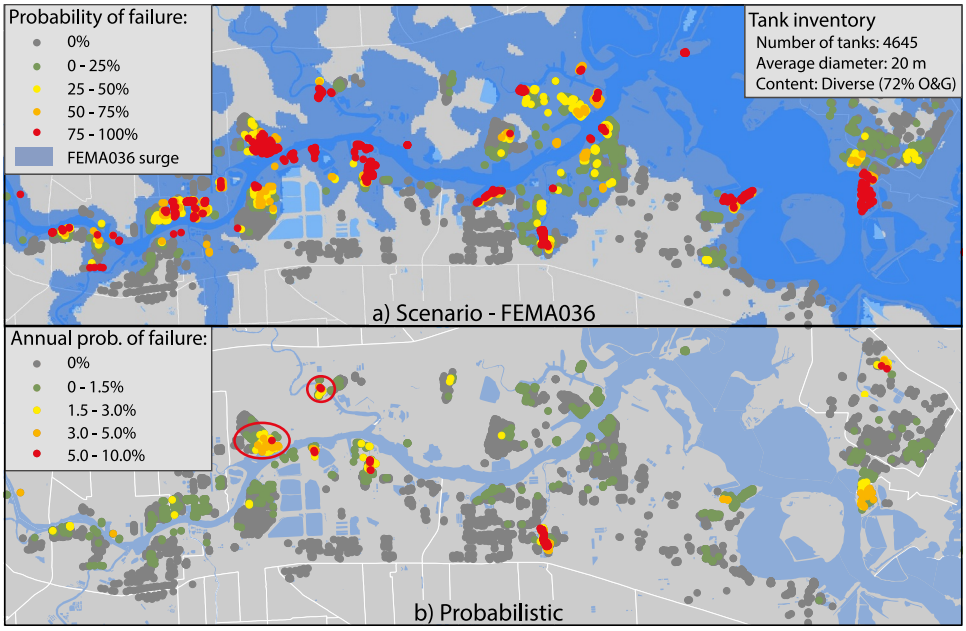

Fig. 7. (a) FEMA036 scenario: Probabilities of being in a failed state at the end of the storm; (b) Probabilistic risk assessment: annual probabilities of failure.

Table 4
Results of the scenario-based and probabilistic risk assessments.

Loads considered	Scenario – FEMA036		Probabilistic	
	$E[SV]$[a] (10^6 liters)	ASTs with P_f > 0.75	1-yr $E[SV]$ (10^6 liters)	20-yr $E[SV]$ (10^6 liters)
All ASTs				
Surge height only	416	609	5.7	48.1
Surge and waves	464	723	6.0	52.9
Surge, wave, and wind	469	733	–	–
Surge, current, wave, and wind	470	733	–	–
ASTs with D > 25 m (30% of ASTs)				
Surge height only	297	57	3.8	32.4
Surge and waves	320	61	3.9	33.6
Surge, wave, and wind	320	62	–	–
Surge, current, wave, and wind	320	62	–	–

[a] $E[SV]$ = Expected spill volume.

Table 5
Performance of the storm hazard surrogate models.

Model	Mean error (%)	R^2
Surge height ($S(\boldsymbol{\omega})$)	2.4	0.98
Significant wave height ($H_s(\boldsymbol{\omega})$)	7.6	0.96
Peak wave period ($T_p(\boldsymbol{\omega})$)	6.8	0.92

$$P(\text{Failure}|\mathbf{X}_1) = \int_{\Omega}\left(\sum_{\delta=\{low,high\}}\mu_{\delta}(x_o)\left(\int_{\mathbf{X}_2}P(\text{Failure}|\mathbf{IM}(\omega),\mathbf{X}_1,\mathbf{x}_2)f_{\mathbf{X}_2}(\mathbf{x}_2)d\mathbf{x}_2\right)f_{\Omega}(\omega|\delta)P(\delta)\right)d\omega \quad (12)$$

As indicated by the summation operator, Eq. (12) distinguishes low intensity storms (28 mb < $\Delta_p \leq$ 48 mb) and high intensity storms (Δ_p > 48 mb) given their significantly different JPDs of storm parameters. In this equation, $\mu_{\delta=low}(x_o)$ and $\mu_{\delta=high}(x_o)$ are respectively the annual rate of occurrence of low and high intensity storms and are a function of the storm landfall location; $f_{\Omega}(\boldsymbol{\omega}|\delta = low)$ and $f_{\Omega}(\boldsymbol{\omega}|\delta = high)$ are the JPDs of storm parameters for low and high intensity storms; $P(\delta)$ is a factor to address the occurrence of low and high intensity storms with $P(\delta = low) = \mu_{\delta=low}/(\mu_{\delta=low} + \mu_{\delta=high})$ and $P(\delta = high) = \mu_{\delta=high}/(\mu_{\delta=low} + \mu_{\delta=high})$; and $\boldsymbol{IM}(\boldsymbol{\omega}) = \{S(\boldsymbol{\omega}) + \varepsilon_S(\boldsymbol{\omega}), H_w(\boldsymbol{\omega}), T_w(\boldsymbol{\omega})\}$ is the set of load parameters at the AST location. While $S(\boldsymbol{\omega}) + \varepsilon_S(\boldsymbol{\omega})$ is evaluated directly from the surge height Kriging model, $H_w(\boldsymbol{\omega})$ and $T_w(\boldsymbol{\omega})$ are obtained from $H_s(\boldsymbol{\omega}) + \varepsilon_{Hs}(\boldsymbol{\omega})$ and $T_p(\boldsymbol{\omega}) + \varepsilon_{Tp}(\boldsymbol{\omega})$ as in Section 6.1; the presence of containment berms is also taken into account when evaluating loads. The error terms $\varepsilon_S(\boldsymbol{\omega})$, $\varepsilon_{Hs}(\boldsymbol{\omega})$, and $\varepsilon_{Tp}(\boldsymbol{\omega})$ propagate the uncertainties associated with the Kriging surrogate models; the error is normally distributed with zero mean and standard deviation $\sigma(\boldsymbol{\omega})$ [59]. For the JPDs of storm parameters, the landfall location (x_o) is modeled as a uniform distribution, the pressure deficit (Δ_p) as a truncated Weibull distribution, the radius of maximum wind (R_m) as a lognormal distribution, and the storm heading (ϕ) and forward speed (V_f) as normal distributions. In addition to the dependence on storm intensity, the parameters of the probability distributions of Δ_p, R_m, ϕ, and V_f are dependent on the landfall location. The actual values of $f_{\Omega}(\boldsymbol{\omega}|\delta = low)$, $f_{\Omega}(\boldsymbol{\omega}|\delta = high)$, $\mu_{\delta=low}(x_o)$, and $\mu_{\delta=high}(x_o)$ employed in this study were provided directly by the USACE [57].

To estimate the annual probability of failure of an AST, Eq. (12) is evaluated using MCS and 10,000 samples. For a given MCS sample, the landfall location is first sampled. The JPDs of storm parameters are then assembled, and a low intensity and high intensity storms are sampled accordingly. For each storm, the hazard intensities are estimated using the Kriging models, the probability of failure of the AST is computed using Eq. (11), and the results are multiplied by the corresponding annual rate of occurrence. Lastly, the weighted average of the low and high intensity storm probabilities of failure is computed using $P(\delta)$. The average over all MCS samples gives the annual probability of failure. Similarly, the annual expected spill volume is evaluated by introducing the internal liquid volume in Eq. (12). Given the limitation of the hazard models, the probabilistic risk assessment is only performed for the maximum storm surge and corresponding wave conditions, neglecting time-dependent effects.

Fig. 7b provides a more comprehensive view of ASTs' vulnerability than Fig. 7a, since it provides the likelihood of failure during a given year considering the likelihood of occurrence of a range of events,

rather than for a single scenario. This information can help support the implementation of risk mitigation plans by identifying more objectively vulnerable ASTs. Nonetheless, scenario-based assessments are still useful for efficient communications with stakeholders and to illustrate the consequence of a hypothetical worst-case event. From Fig. 7b, it is possible to identify a few clusters of ASTs with relatively high annual probability of failure (> 3%). Interestingly, two of these clusters (circled in red in Fig. 7b) correspond to the locations of the two main dislocation-related AST spills during Hurricane Harvey in 2017 [2], further highlighting the worthiness of the tools developed here.

The effects of wave loads in the probabilistic risk assessment are also detailed in Table 4. Wave loads only increase the annual expected spill volume by 5% since storms generating severe wave conditions have a small probability of occurrence. However, if the risk assessment is performed for a longer time horizon, such as 20 years, the effect of wave loads becomes more important as storms with significant wave conditions are more likely to occur over 20 years than one year. As shown in Table 4, wave loads can increase the expected spill volume by 10% in such case. The rates of occurrence in Eq. (12) were adjusted to a 20-year horizon by assuming that the occurrence of storms follows a Poisson process. These results again highlight the importance of considering the multi-hazard nature of storms to adequately assess the risks of ASTs in coastal areas.

7. Summary and conclusions

This paper aimed to develop a rigorous, yet efficient, methodology to perform fragility and risk assessments of ASTs subjected to concurrent storm surge, wave, and wind loads. First, a surrogate model was developed to accurately and efficiently estimate storm surge and wave loads on ASTs in place of complex and expensive CFD analyses. A comprehensive framework that propagates modeling and epistemic uncertainties was then presented to estimate AST buckling strength and stability against dislocation when subjected to multi-hazard storm conditions. Using a statistical sampling method and logistic regression, the first fragility models for ASTs subjected to multi-hazard storm conditions were derived for buckling and dislocation. To facilitate their future adoption, the fragility models were parametrized on modeling parameters and load conditions, and can be readily employed to assess the vulnerability of any ASTs subjected to realistic surge, wave, and wind conditions.

By illustrating their usage for two case study ASTs, the fragility models also provided useful insights regarding the vulnerability of ASTs. Overall results indicated that the concurrent effects of surge, wave, and wind loads were of paramount importance to adequately assess the structural vulnerability of ASTs during storm events. Focusing on a single hazard, as existing studies have generally done, can result in a significant underestimation of the probability of failure. For instance, neglecting wave loads for ASTs subjected to storm surge can underestimate the probability of failure by up to 40%. For wind loads, the effect on structural vulnerability is more limited but can still be significant for high wind velocities that are above the design value.

To gain further insights on the vulnerability of ASTs, this study also performed risk assessments of ASTs located in a large industrial area and subjected to realistic storm conditions. A first risk assessment was performed by coupling the derived fragility models with a severe deterministic storm scenario. A second risk assessment, consisting of the first probabilistic risk assessment of ASTs in storm prone regions, was also performed. To facilitate the probabilistic assessment, a computationally efficient surrogate model based on a limited set of storm simulations was derived to evaluate storm surge and wave conditions at AST locations. The two risk assessments revealed that while storm surge is the most important load, considering multi-hazard conditions is essential to adequately assess vulnerability and risks, especially when looking at severe events or long-term horizons. Again, the effect of wave loads was shown to be more significant than wind loads. Lastly, compared to the scenario-based assessment and existing studies, which have been limited to scenario assessments, the probabilistic risk assessment was found to provide more comprehensive measures of risks that capture the uncertainties associated with storm variability and occurrence.

Overall, this study provided methods, tools, and insights essential to evaluate the resilience of a key energy infrastructure and support industry managers in developing adequate mitigation plans. Moreover, this study highlighted the benefits of developing surrogate models to facilitate and reduce the computational complexity of fragility and risk assessments across regional portfolios. The tools and methods presented here can be adapted to other industrial and energy infrastructure located in coastal areas prone to storm events. Although this study focused on individual ASTs, future work should look at the vulnerability of ASTs in groups, as group effects could modify loads acting on ASTs. Additional future work should investigate the correlation and interactions between the different failure modes, as well as more severe hydrodynamic conditions such as breaking and focused waves.

Acknowledgments

The authors acknowledge the support of this research by the National Science Foundation under award CMMI-1635784. The contributions of the first author were supported in part by the Natural Sciences and Engineering Research Council of Canada. The authors thank Prof. Clint Dawson, Dr. Giannis Gidaris, and the US Army Corps of Engineering for providing the *ADCIRC + SWAN* and storm data. Any opinions, findings, and conclusions or recommendations expressed herein are those of the authors and do not necessarily reflect the views of the sponsors.

Supplementary materials

Supplementary material associated with this article can be found, in the online version, at doi:10.1016/j.ress.2019.106571.

References

[1] Godoy L. Performance of storage tanks in oil facilities damaged by Hurricanes Katrina and Rita. J Perform Constr Facil 2007;21:441–9.
[2] Bernier C, Padgett JE. Forensic investigation of aboveground storage tank failures during Hurricane Harvey using fragility models. Forensic Eng. 8th Congr. 2018.
[3] Cozzani V, Campedel M, Renni E, Krausmann E. Industrial accidents triggered by flood events: analysis of past accidents. J Hazard Mater 2010;175:501–9.
[4] Necci A, Girgin S, Krausmann E. Understanding Natech risk due to storms - lessons learned and recommendations. 2018.
[5] Masoomi H, Van De Lindt JW, Ameri MR, Do TQ, Webb BM. Combined wind-wave-surge hurricane-induced damage prediction for buildings. J Struct Eng 2018;145:1–15.
[6] Suarez-Paba MC, Perreur M, Munoz F, Cruz AM. Systematic literature review and qualitative meta-analysis of Natech research in the past four decades. Saf Sci 2019;116:58–77.
[7] Krausmann E, Cruz AM, Salzano E. Natech risk assessment and management: reducing the risk of natural-hazard impact on hazardous installations. Elsevier; 2016.
[8] Krausmann E. Natural hazard triggered technological (Natech) accidents - an overlooked type of risk ? Loss Prev Bull 2016;250:11–5.
[9] Cruz AM, Krausmann E. Vulnerability of the oil and gas sector to climate change and extreme weather events. Clim Change 2013;121:41–53.
[10] Buratti N, Tavano M. Dynamic buckling and seismic fragility of anchored steel tanks by the added mass method. Earthq Engng Struct Dyn 2014;43:1–21.
[11] Phan HN, Paolacci F, Alessandri S. Enhanced seismic fragility analysis of unanchored steel storage tanks accounting for uncertain modeling parameters. J Press Vessel Technol 2018.
[12] Cortes G, Prinz GS. Seismic fragility analysis of large unanchored steel tanks considering local instability and fatigue damage. Bull Earthq Eng 2017;15:1279–95.
[13] Kabir G, Suda H, Cruz AM, Giraldo FM, Tesfamariam S. Earthquake-related Natech risk assessment using a Bayesian belief network model. Struct Infrastruct Eng 2019:2479.
[14] D'Amico M, Buratti N. Observational seismic fragility curves for steel cylindrical tanks. J Press Vessel Technol 2018;141:010904.
[15] Necci A, Antonioni G, Cozzani V, Krausmann E, Borghetti A, Alberto Nucci C. A model for process equipment damage probability assessment due to lightning. Reliab Eng Syst Saf 2013;115:91–9.
[16] Necci A, Antonioni G, Bonvicini S, Cozzani V. Quantitative assessment of risk due to

major accidents triggered by lightning. Reliab Eng Syst Saf 2016;154:60–72.
[17] Wu D, Chen Z. Quantitative risk assessment of fire accidents of large-scale oil tanks triggered by lightning. Eng Fail Anal 2016;63:172–81.
[18] Basco A, Salzano E. The vulnerability of industrial equipment to tsunami. J Loss Prev Process Ind 2017;50:301–7.
[19] Mebarki A, Jerez S, Prodhomme G, Reimeringer M. Natural hazards, vulnerability and structural resilience: tsunamis and industrial tanks. Geomatics, Nat Hazards Risk 2016;7:5–17.
[20] Godoy LA. Buckling of vertical oil storage steel tanks: review of static buckling studies. Thin-Walled Struct 2016;103:1–21.
[21] Kameshwar S, Padgett JE. Storm surge fragility assessment of above ground storage tanks. Struct Saf 2018;70:48–58.
[22] Landucci G, Antonioni G, Tugnoli A, Cozzani V. Release of hazardous substances in flood events: damage model for atmospheric storage tanks. Reliab Eng Syst Saf 2012;106:200–16.
[23] Khakzad N, Van Gelder P. Vulnerability of industrial plants to flood-induced natechs: a Bayesian network approach. Reliab Eng Syst Saf 2018;169:403–11.
[24] Khakzad N, Van Gelder P. Fragility assessment of chemical storage tanks subject to floods. Process Saf Environ Prot 2017;111:75–84.
[25] Kameshwar S, Padgett JE. Fragility and resilience indicators for portfolio of oil storage tanks subjected to hurricanes. J Infrastruct Syst 2018;24:04018003.
[26] Mayorga SZ, Sánchez-Silva M, Olivar OJR, Giraldo FM. Development of parametric fragility curves for storage tanks: a Natech approach. Reliab Eng Syst Saf 2019;189:1–10.
[27] Antonioni G, Landucci G, Necci A, Gheorghiu D, Cozzani V. Quantitative assessment of risk due to Natech scenarios caused by floods. Reliab Eng Syst Saf 2015;142:334–45.
[28] Masoomi H, Ameri MR, van de Lindt JW. Wind performance enhancement strategies for residential wood-frame buildings. J Perform Constr Facil 2018;32:04018024.
[29] Tomiczek T, Kennedy A, Rogers S. Collapse limit state fragilities of wood-framed residences from storm surge and waves during Hurricane Ike. J Waterw Port, Coastal, Ocean Eng 2013;140:43–55.
[30] Do TQ, van de Lindt JW, Cox DT. Performance-based design methodology for inundated elevated coastal structures subjected to wave load. Eng Struct 2016;117:250–62.
[31] Wei K, Arwade SR, Myers AT, Hallowell S, Hajjar JF, Hines EM, et al. Toward performance-based evaluation for offshore wind turbine jacket support structures. Renew Energy 2016;97:709–21.
[32] Dietrich JC, Tanaka S, Westerink JJ, Dawson CN, Luettich RA, Zijlema M, et al. Performance of the Unstructured-Mesh, SWAN+ADCIRC model in computing hurricane waves and surge. J Sci Comput 2012;52:468–97.
[33] Ebersole BA, Massey TC, Melby JA, Nadal-Caraballo NC, Hendon DL, Richardson TW, et al. Interim report - Ike Dike concept for reducing hurricane storm surge in the Houston-Galveston region. 2016. Jackson, MS.
[34] American Society of Civil Engineers. ASCE7-16 - Minimum design loads and associated criteria for buildings and other structures. 2017.
[35] Chen L, Rotter JM. Buckling of anchored cylindrical shells of uniform thickness under wind load. Eng Struct 2012;41:199–208.
[36] Bu F, Qian C. A rational design approach of intermediate wind girders on large storage tanks. Thin-Walled Struct 2015;92:76–81.
[37] European Committee for Standardization. Eurocode 3: design of steel structures—Part 4-1: design of steel structures: silos (EN 1993-4-1). Brussels, Belgium: 2007.
[38] Sumer BM, Fredsoe J. Hydrodynamics around cylindrical strucures 26. World scientific; 2006.
[39] Hu ZZ, Greaves D, Raby A. Numerical wave tank study of extreme waves and wave-structure interaction using OpenFoam®. Ocean Eng 2016;126:329–42.
[40] Bernier C, Padgett J. Buckling of aboveground storage tanks subjected to storm surge and wave loads. Eng Struct 2019. (accepted; in press).
[41] Livermore Software Technology Corporation. LS-Dyna R8.0.0. 2016.
[42] Fenton JD. Use of the programs FOURIER, CNOIDAL and STOKES for steady waves. 2015. Vienna, Austria.
[43] Mckay MD, Beckman RJ, Conover WJ. A comparison of three methods for selecting values of input variables in the analysis of output from a computer code. Technometrics 1979;21:239–45.
[44] Bernier C, Elliott JR, Padgett JE, Kellerman F, Bedient PB. Evolution of social vulnerability and risks of chemical spills during storm surge along the Houston Ship Channel. Nat Hazards Rev 2017;18:1–14.
[45] Gavalda X, Ferrer-Gener J, Kopp GA, Giralt F. Interpolation of pressure coefficients for low-rise buildings of different plan dimensions and roof slopes using artificial neural networks. J Wind Eng Ind Aerodyn 2011;99:658–64.
[46] Bernier C, Padgett JE. Neural network for estimating storm surge loads on storage tanks. 13th Int. Conf. Appl. Stat. Probab. Civ. Eng., Seoul, South Korea. 2019.
[47] Bernier C. Fragility and risk assessment of aboveground storage tanks during storm events. Rice University; 2019.
[48] American Petroleum Institute. API standard 650: welded tanks for oil storage. twelfth ed. 2013.
[49] Kildashti K, Mirzadeh N, Samali B. Seismic vulnerability assessment of a case study anchored liquid storage tank by considering fixed and flexible base restraints. Thin-Walled Struct 2018;123:382–94.
[50] Kameshwar S, Padgett JE. Stochastic modeling of geometric imperfections in aboveground storage tanks for probabilistic buckling capacity estimation. ASCE-ASME J Risk Uncertain Eng Syst, Part A Civ Eng 2015;2.
[51] Sosa EM, Godoy LA. Nonlinear dynamics of above-ground thin-walled tanks under fluctuating pressures. J Sound Vib 2005;283:201–15.
[52] Eligehausen R, Mallee R, Silva JF. Anchorage in concrete construction. Wiley; 2006.
[53] Rabbat BG, Russell HG. Friction coefficient of steel on concrete or grout. J Struct Eng 1985;111:505–15.
[54] Leonards G. Experimental study of static and dynamic friction between soil and typical construction materials. 1965.
[55] Elfrink B, Hanes DM, Ruessink BG. Parameterization and simulation of near bed orbital velocities under irregular waves in shallow water. Coast Eng 2006;53:915–27.
[56] World Meteorological Organization. Guidelines for converting between various wind averaging periods in tropical cyclone conditions. 2010.
[57] Melby JA, Nadal-caraballo N, Ratcliff JJ, Massey TC, Jensen RE. Sabine pass to galveston bay wave and water level modeling. 2015. Vicksburg, MS.
[58] Jia G, Taflanidis AA. Kriging metamodeling for approximation of high-dimensional wave and surge responses in real-time storm/hurricane risk assessment. Comput Methods Appl Mech Eng 2013;261–262:24–38.
[59] Lataniotis C, Marelli S, Sudret B. UQLab user manual - Kriging. 2018.